47th AIAA Aerospace Sciences Meeting Including The New Horizons Forum and Aerospace Exposition
5 - 8 January 2009, Orlando, Florida
AIAA 2009-1221

# Unstructured Mesh CFD Aerodynamic Analysis of the NREL Phase VI Rotor

Mark A. Potsdam*
*Aeroflightdynamics Directorate (AMRDEC), U.S. Army Research, Development and Engineering Command*
*University of Wyoming Wind Energy Research Center*
*Moffett Field, CA 94035*

Dimitri J. Mavriplis†
*Wind Energy Research Center*
*University of Wyoming*
*Laramie, WY 82071*

**An unstructured mesh Navier-Stokes computational fluid dynamics solver NSU3D is evaluated for wind turbine aerodynamic predictions and comparisons are made with the NREL Phase VI Unsteady Aerodynamics Experiment (UAE). Calculations use isolated rotor steady-state and unsteady, time-accurate formulations. A range of unstructured surface mesh densities and topologies are investigated. Adaptive mesh refinement for wake capturing is evaluated for accuracy requirements. Comparison of rotor performance, aerodynamic spanload distributions, surface pressures, and flow visualization are made against available wind tunnel data and a structured overset grid flow solver OVERFLOW.**

## I. Introduction

With a U.S. scenario to produce 20% of its energy needs with wind energy by 2030, it is recognized that one of the major challenges is technology advancement for reduction in wind capital costs and improvements in turbine performance [27]. This requires continued validation of new and existing design tools and increased accuracy and efficiency of the results. Aerodynamically, this implies not only lower-order multidisciplinary tools but also use of advanced high fidelity methodologies such as coupled computational fluid dynamics (CFD) and structural dynamics (CSD). CFD methods offer the opportunity for advances in airfoil and blade aerodynamics, rotor performance, aeroacoustics, aeroelastics, wind farm design, and wind turbine siting. CFD and wind tunnel testing can be used in a complementary manner to better understand the fundamental fluid dynamics phenomena involved in wind turbine aerodynamics, such as boundary layer transition, dynamic stall, inflow turbulence, active control methods, and three-dimensional effects.

At the University of Wyoming, a Wind Energy Research Center (WERC) has been established to perform research into issues related to wind energy, especially in specialized areas of ongoing activities, including atmospheric sciences, unsteady experimental fluid dynamics, controls, nonlinear structural mechanics, small wind, and high fidelity computational aeroelasticity. The computational capability stems from ongoing work on CFD algorithm development, aerodynamic optimization, transonic drag prediction capability, and cooperation with the U.S. Army in the field of rotorcraft CFD. The significant wind resources, and energy resources in general, as well as the academic expertise in Wyoming and at the University make it a logical center for fundamental research and development activities in wind energy.

High fidelity Navier-Stokes computational fluid dynamics is currently making inroads into many phases of industrial wind energy design [16,17]. Engineers are using CFD for both 2D airfoil [5,16,24,25] and 3D blade analysis and design. Airfoils tables of lift, drag, and pitching moment from the 2D analyses are used in blade element models (BEM), which are still the workhorse within multidisciplinary wind turbine analyses due to their high efficiency over CFD methods when hundreds of load cases must be performed. However, BEM models are dependent on empirical corrections to 2D airfoil tables to account for 3D effects, such as tip loss, rotational flow,

* Aerospace Engineer, Aeromechanics Division, M/S 215-1, Senior Member, mark.potsdam@us.army.mil
† Professor, Department of Mechanical Engineering, Associate Fellow, mavripl@uwyo.edu.



This material is declared a work of the U.S. Government and is not subject to copyright protection in the United States.

and dynamic stall. High fidelity CFD naturally includes these phenomena, but has more difficulty modeling other wind turbine phenomena such as variable turbulent inflow and boundary layer transition [18]. CFD has been used to improve the aerodynamic design of wind turbines including tip shapes, winglets, and hub modeling [19,20,21,26] where it has high potential in areas where BEM models are no longer applicable. Nacelle and tower integration [8] and terrain modeling are also being performed [16,17].

The NREL Phase VI Unsteady Aerodynamic Experiment [1,2,23] provides an excellent validation test case for computational fluid dynamics analyses. The Phase VI test campaign performed in the NASA Ames National Full-Scale Aerodynamic Complex (NFAC) was completed in 2000. The 2-bladed, 10 m diameter, stall regulated turbine has a power rating of 20kW. The blades are twisted and mildly tapered. Multidisciplinary measurements were obtained over a wide range of operating conditions. Experimental measurements included blade pressures and resulting integrated airloads, shaft torque, sectional inflow conditions, blade root strain, tip acceleration and wake visualization. Both upwind and downwind configurations with rigid and teetering blades were run for speeds from 5 to 25 m/s. Yawed and unsteady pitch configurations are also available. Free and fixed transition results were measured. The blade uses specially designed S809 airfoils for which experimental aerodynamic performance parameters are available. Blade structural properties are well documented.

Numerous researchers [3,4,5,6,7,8,22,23,28,29] have investigated this configuration numerically using a range of CFD methods and grid topologies. Much of the numerical analysis was a blind comparison pre-test prediction [23] using a very large range of performance, aeroelastic, and CFD codes. Results from this study indicated that there was a wide variation in the prediction capability. Comparisons with wind tunnel data were generally “not favorable”. During the blind comparison, Duque used the overset grid steady-state Navier-Stokes solver OVERFLOW-D and the Baldwin-Barth turbulence model on the configuration [3]. Resulting torque predictions were quite good in both the attached flow and stalled regions. Researchers at the University of California at Davis have more recently used the updated OVERFLOW 2.0 to investigate flatback airfoils on the Phase VI configuration [4]. Their work included unsteady configurations and low Mach number preconditioning. Torque was overpredicted at the start of the stalled regime. Le Pape at ONERA used the multiblock Navier-Stokes solver elsA to compute the 2D airfoil and 3D blade performance using both steady and unsteady formulations [5]. Rotor torque in the stalled regime was underpredicted using the k-ω SST turbulence model although the stall initiation was exceptionally well captured in both 2D and 3D. Researchers at Risø computed the isolated rotor with and without wind tunnel walls using a multiblock, structured mesh, incompressible solver EllipSys3D with a RANS turbulence model [28] and a detached eddy simulation [29]. Performance was generally well captured although stall initiation at 10 m/s wind speed was missed. Zahle at Risø used the overset, structured mesh incompressible solver EllipSys3D to model the rotor and tower configurations [8]. Rotorcraft wake adaption in hover with an unstructured solver has been developed at KAIST (e.g. Ref. 37), where wake vorticity detection and vortex tracking are used to generate a seven level adapted mesh starting from a coarse initial solution.

The objective of the current work is to validate an efficient mixed element unstructured grid Navier-Stokes solver (NSU3D), including adaptive mesh refinement (AMR), on the NREL Phase VI wind turbine dataset. The paper is organized as follows: the Methodology section begins with a description of the computational fluid dynamics flow solver NSU3D including the steady and unsteady discretizations for an isolated rotor. The unstructured grid adaption methodology is described. A short description of the overset mesh, structured solver OVERFLOW, which is used for comparison, is also given. Then computational results are presented for the NREL Phase VI rotor with experimental data from the Unsteady Aerodynamic Experiment (UAE) wind tunnel test data base. Computational NSU3D and OVERFLOW results are presented for the unyawed, upwind rotor configuration for a range of wind speeds. NSU3D results are presented with a 1) non-inertial steady formulation which includes additional momentum source terms 2) an unsteady time-accurate formulation, and 3) a non-inertial steady formulation using grid adaption for wake capturing. The effects of grid density and topology are studied in detail for the non-inertial steady formulation. Comparisons are made with OVERFLOW and experimental results for rotor performance (thrust and power), aerodynamic spanload distributions, and surface pressures. Flow visualizations are also investigated. Finally, a summary of the findings and relevant conclusions are presented.

## II. Methodology

### A. NSU3D Unstructured Mesh Flow Solver

The NSU3D code [9,10,11] is an unstructured mesh multigrid Reynolds-averaged Navier-Stokes (RANS) solver for high Reynolds number external aerodynamic applications. The NSU3D discretization employs a vertex-based approach, and fluxes are computed on faces delimiting dual control volumes, with each dual face being associated

with a mesh edge. This discretization operates on hybrid mixed element meshes, generally employing prismatic elements in highly stretched boundary layer regions and tetrahedral elements in isotropic regions of the mesh away from the solid surfaces. A single edge-based data structure is used to compute flux balances across all types of elements. The convective terms are discretized as central differences with added matrix dissipation. Second-order accuracy is achieved by formulating these dissipative terms as an undivided biharmonic operator, which is constructed in two passes of a nearest neighbor Laplacian operator. In the matrix form, this dissipation is similar to that produced by a Riemann solver gradient-based reconstruction scheme, and is obtained by replacing the difference in the reconstructed states on each side of the control volume interface by the undivided differences along mesh edges resulting from the biharmonic operator construction. These differences are then multiplied by the characteristic matrix to obtain the final dissipation terms. A Roe upwind scheme using least-squares gradient reconstruction has also been implemented.

The baseline NSU3D viscous discretization employs a finite-difference scheme to approximate the thin-layer form of the viscous terms for the Navier-Stokes equations, although this is done in a multidimensional fashion, by computing a Laplacian of the velocity field. The main approximation in this approach is the omission of the cross-derivative viscous terms, and the assumption of a locally constant viscosity. The discretization of the full Navier-Stokes terms has also been implemented but is not used here. Turbulence closure is provided by the Spalart-Allmaras turbulence model, although k-ω and the Menter SST model are also available. The approximate S-A model with rotation and curvature (ASARC) is also implemented [31]. Although rotorcraft hover calculations can show considerable improvement performance prediction when some form of the rotation and curvature corrections are applied, no difference was seen in the current calculations, and the modified ASARC model is not used.

The basic time-stepping algorithm in NSU3D consists of a three-stage explicit scheme. Convergence is accelerated by a local block-Jacobi preconditioner in regions of isotropic grid cells. In boundary layer regions, where the grid is highly stretched, a line preconditioner is employed to relieve the stiffness associated with the mesh anisotropy. An agglomeration multigrid algorithm is used to further enhance convergence to steady state. The Jacobi and line preconditioners are used to drive the various levels of the multigrid sequence, resulting in a rapidly converging solution technique. In the time-accurate formulation, NSU3D employs a second-order backward difference (BDF2) scheme for temporal accuracy. At each time step the steady-state scheme described is used to subiterate in pseudo-time.

For transonic flows, for which the flow solver has been particularly optimized, the solver is generally run 500-1000 multigrid cycles. However, low speed and isolated rotor cases in hover and low wind speed have been seen to require significantly more cycles. Low Mach preconditioning (LMP) was not used for the current calculations, although the use of LMP would most likely benefit convergence and accuracy in the wind turbine flow regime [4,5]. The current steady-state LMP implementation is probably not correct for moving grids, as the grid speed must be included in the local preconditioning parameter [30]. Further work in this area is required for validation. In all the steady-state cases, two levels of multigrid are used along with initial grid sequencing. Using the non-inertial steady-state isolated rotor formulation, solutions typically require six to fifteen thousand iterations.

A no slip boundary condition is used on the rotor surfaces, taking into account the surface speed of the rotating blade. For flow visualization purposes, results are shown in the non-inertial, rotating frame of reference. A Dirichlet boundary condition is used on all the outer boundaries. Because of the ghost cell boundary condition formulation, the fixed freestream boundary values are only weakly enforced. Grid speeds for the steady and unsteady formulations are constructed along edges and satisfy the Geometric Conservation Law (GCL) [36].

### B. Unstructured Mesh Generation

A variety of unstructured surface grid topologies have been investigated in an attempt to determine the most accurate and efficient mesh generation approach for high aspect ratio wind turbine blades. The surface topologies are (1) structured multiblock with quadrilateral elements (2) fully unstructured triangular, (3) mixed element triangular and quadrilateral. The surface mesh topologies are shown in Figure 1. For the topologies with quadrilateral surface meshes (1 and 3), each quad has been further subdivided into two triangular faces during the volume grid generation process so that there are no hexahedral elements in the unstructured meshes, only prisms, pyramids, and tetrahedra.

The multiblock surface mesh (1) was extracted directly from the original surface definition provided as a structured mesh. However, the tight trailing edge spacing results in cells aspect ratios over 1000 in the center of the blade and order 100 near the tip. Since these large aspect ratio surface cells pose significant difficulties for unstructured, viscous volume grid generation, every other grid line in the streamwise direction was extracted (Figure 1-1). Even so, the leading edge spacing is 0.0012c, the trailing edge spacing is .00048c, and the cell aspect ratios

approach 500 in the mid-span trailing edge region. The surface topology is generally an O-grid along most of the blade, with 65 points chordwise on the upper and lower surfaces (each) and 65 points spanwise.

The two unstructured surface meshes (2,3) were generated using the Pointwise software [13]. The leading and trailing edge chordwise spacings for these meshes is a constant 0.003 m, which ranges from .0043c at the root to .0085c at the tip. There are 71 points along the upper and lower surfaces in the streamwise direction. Spanwise the spacings are .0012R at the root and .0007R at the tip. The fully unstructured grid (2) is made up of generally equilateral triangles as Pointwise has no capability to generate stretched triangles. The lack of stretching in the fully triangular surface mesh makes high resolution exceedingly expensive. There are 651 points in the spanwise direction along the leading and trailing edges. However, the point spacings from the root, tip. leading and trailing edge lines are seen not to filter into the interior of the blade surface so the resolution is reduced (Figure 1-2). The mixed topology mesh (3) is triangular in the tip and root regions, but a large percentage of the span is made up of structured quadrilateral cells (Figure 1-3). There are 181 points spanwise. Since the mixed topology mesh allows cell stretching, a more reasonable cell count is possible along with better resolution. The maximum surface cell aspect ratio for the mixed element surface mesh is limited to approximately 10 at the mid-span. The cell spacings are also maintained all along the blade span, unlike in the fully triangular surface mesh. Finer version of both the triangular and mixed element surface meshes were generated with half the spacing and double the number of points everywhere.

Volume grid generation was performed using the Simcenter Advancing Front with Local Reconnection (AFLR3) software by David Marcum at Mississippi State University [14]. The normal spacing at the wall is $6x10^{-6}$ m for a $y^+ < 1$ on most of the blade. Prism cells are generated in the viscous layer region near the wall out to a distance based on a calculated boundary layer thickness and achieve a smooth transition with the tetrahedral region, although the extent of the generated prism layer is seen to vary based on surface resolution. Cuts through the volume grids are shown in Figure 2. Tetrahedral cells fill the remainder of the domain out to the farfield, which is located at six rotor radii. For the fine mixed element surface mesh, a grid with reduced normal spacing was also generated.

The AFLR3 volume grid spacing is determined based on interpolation of surface spacings. In order to decrease the cell sizes in the wake region, a source wake surface is inserted in the volume grid generation. This wake sheet is shown in Figure 3a and is seen to influence the volume distributions in the unstructured AFLR3 mesh downstream of the rotor (Figure 3b). The wake sheet is not present in the final mesh and is merely a device for point clustering.

The overall grids and sizes are summarized in Table 1. Note that due to the use of mixed element volume meshes, the element to node ratio is noticeably lower (~2.5) compared with an all tetrahedral mesh (~5.5).

### C. Unstructured Mesh Adaption

An adaptive refinement strategy based on hierarchical element subdivision has been formulated and implemented for meshes containing arbitrary mixes of tetrahedra, hexahedra, prisms and pyramids [12]. The methodology subdivides edges based on an adaption criteria. In order to implement this technique on mixed meshes, the various allowable subdivision types must be predefined. For tetrahedra, hexahedra, prisms, and pyramids, there are currently 3, 8, 9, and 8 refinement patterns, respectively. Although this is not a complete list of possible refinements, it is a minimal number required for compatible subdivision without unwanted excessive refinement and to avoid the introduction of additional points at neighboring cell centroids. Compatible refinement patterns on all cells is achieved iteratively. Directional anisotropic refinement is not currently implemented.

The adaptive meshing module is constructed as a separate code from the flow solver with special attention given to keeping memory overheads as low as possible, preferably less than that required by the other mesh preprocessors and the flow solver on a serial processor. The adaptive mesh code reads in a mesh and a solution file generated by the flow solver and outputs a refined mesh and interpolated solution file. This is then read in by the flow solver for the next solution adaption level. In place of the input solution file, an adaption preprocessor can read the solution file and output any desired quantity. The adaption criteria preprocessor is necessary for constructing complex gradient functions since all the required data structures are not available within the adaption routines for this purpose. In this case an interpolated flow solution file for flow solver restart may not be available on output. In the present procedure, only the required data structures for each module (mesh preprocessors, adaption code, and flow solver) are resident in memory, and the modules communicate through file I/O. This procedure can easily be automated using a scripting language.

Adaption criteria are based on differences of variables along edges compared with a norm. In order to ensure isotropic refinement patterns, when one edge of a mesh element is initially flagged for refinement, all other edges of the element are flagged and the element becomes fully refined isotropically. In the final adapted mesh, only transition elements between fully refined and non-refined regions contain anisotropically subdivided elements. Of

ongoing research is the appropriate quantity to use for adaption or error estimation, especially for subsonic vortical flows without shocks. Transonic fixed wing calculations have used the undivided density along an edge. The flow solver adjoint has also been employed to specify adaption based on a desired output quantity (e.g. drag). The Q criteria [15] has been found to efficiently capture a vortex-dominated wake without excessively highlighting the wall-bounded viscous flows, which would tend to be adapted based on a more conventional vorticity criteria. For this work adaption criteria based on function values at the edge midpoint have been implemented.

If surface adaption is performed, the added points must be made to conform to the surface as linear interpolation along an edge is a poor approximation. A procedure is used to project the new surface points on to a CAD definition of the model. A grid motion routine is then applied to redistribute and smooth the volume grid, especially in the viscous layers.

Using the adaption methodology, inviscid as well as viscous flows have been computed on adaptively refined tetrahedral, hexahedral, and hybrid meshes [12]. The efficiency of the method is demonstrated in Figure 4a by generating an adapted tetrahedral mesh in the wake of a 3-bladed tiltrotor in hover. The tip of a wind turbine blade has been adapted and shows both surface and volume adaption of the mixed element, viscous mesh in Figure 4b.

Numerous difficulties can be encountered during unstructured mesh adaption. After several adaption levels the mesh quality can degrade rather rapidly. It may become necessary to perform mesh smoothing or edge swapping to improve the mesh quality. One particular predicament is that the number of edges associated with a node can become quite large. This can occur, for example, in a vortex where the center of the vortex is not refined because the gradients are low, but surrounding cells are all refined. In this case, cells associated with nodes that have large increases in edge degree can be flagged for further subdivision to improve the situation. Modifications to the undivided biharmonic operator in the NSU3D flow solver is also required to alleviate difficulties associated with nodes of very high edge degree, i.e. much above the average of approximately 14. The Roe scheme with reconstruction does not seem to be similarly affected.

Special attention is also required in boundary layer prism regions. Without the ability to anisotropically refine boundary layer prism elements, excessive node count may result as any refinement of the triangular faces results in normal refinement as well. Given reasonable ability to predict normal spacing and distributions based on the Reynolds number and $y^+$ requirements, it may not be necessary to increase the boundary layer resolution. For flow solver efficiency and robustness, it is desirable to maintain boundary layer lines which are continuous and extend throughout the layer, otherwise the boundary layer grid structure can be easily ruined. These issues have not been addressed here as only off-body tetrahedral wake adaption is performed.

### D. OVERFLOW Overset Structured Mesh Flow Solver

For comparison with the NSU3D calculations, additional CFD calculations have been performed using the Reynolds-averaged Navier-Stokes computational fluid dynamics code OVERFLOW 2.1 [32,33]. The code is continually being developed at NASA and has been applied to a wide range of fluid dynamics problems. OVERFLOW 2 includes capability, integrated from OVERFLOW-D [34], for time-dependent dynamic rigid body motion of components. OVERFLOW-D is an out-of-date, unsupported flow solver based on OVERFLOW 1.6au which was the original development platform for rotorcraft and wind turbine simulations [3]. OVERFLOW solutions are computed on structured, overset grids using body-conforming, curvilinear “near-body” grids and automatically generated Cartesian “off-body” grids in the wake and farfield. The off-body grids are generated by level with grid spacing increased by a factor of two at each level until reaching the outer boundary of the computational domain.

OVERFLOW includes a wide range of options for numerical methods, boundary conditions, and turbulence models. In this work, fourth-order central spatial differencing with second- and fourth difference scalar artificial dissipation is used for the convective terms in both the near- and off-body grids. Steady-state calculations use a scalar pentadiagonal Pulliam-Chaussee algorithm. Viscous modeling is used in the near-body grids along with a turbulence model. For the uniform Cartesian off-body grids, the viscous terms are not included, due to the large grid spacings used relative to an actual vortex core size. OVERFLOW 2 solutions use the Spalart-Allmaras turbulence model, while OVERFLOW-D uses Baldwin-Barth. A no slip surface boundary condition is used on the rotor, and a farfield Riemann condition is used on the outer boundaries.

### E. Structured Grid Generation

The near-body volume grid was generated from the initial overset grid surface definition using the NASA Chimera Grid Tools. The surface topology is generally an O-grid along most of the blade, with 129 points chordwise

on the upper and lower surface (each) and 65 points spanwise, excluding the overlap regions. The leading edge spacing is 0.00060c and the trailing edge spacing is 0.00024c, which are considerably tight. The cell aspect ratios are upwards of 1000 at the trailing edge. The off-body Cartesian grid is automatically generated by OVERFLOW. The smallest off-body spacing is set to 10% of the tip chord (0.34 m). No attempt was made to resolve the wake region in the off-body grid, and only surface proximity is used. Examples of the grid are shown in Figure 1-4, Figure 2-4, and Figure 5. As in the unstructured meshes, the first point off the surface is $6x10^{-6}$ m, which is constant for 3 layers. Due to surface stretching, the OVERFLOW mesh offers twice the volume resolution compared with the coarse unstructured meshes with similar surface point count, especially behind the trailing edge.

### F. Additional Flow Solver Considerations

Both the unstructured (NSU3D) and structured (OVERFLOW) flow solvers use an isolated rotor, steady-state formulation in the non-inertial reference frame, which transforms the unsteady problem into a steady one with the addition of a rotational source term in the momentum equations, while still solving for the inertial velocities in the flowfield [39]. The non-inertial steady-state formulation offers significant efficiency advantages over time-accurate moving blade simulations.

For parallel processing both solvers use the MPI Message Passing Interface. OpenMP is implemented in both solvers but was not used here. In OVERFLOW, domain decomposition is implemented on a grid-by-grid basis, with internal grid splitting possible for improved load balancing. NSU3D uses the graph-based partitioner "Metis" [41] for domain decomposition of the mesh and the associated agglomerated multigrid levels.

## III. NREL Phase VI Configuration

The NREL Phase VI rotor geometry, aerodynamic and structural properties are well-documented in the literature [1,2]. The geometry used here was obtained from Dr. Earl Duque [3] and has been developed in cooperation with Risø [28]. The basis for the geometry is in the form of a fine overset structured surface mesh. The theoretical definition of the S809 airfoil has a very sharp trailing edge. The geometry used here appears to originally have had a blunt trailing edge that has been closed off over the last approximately 1% of the chord. This introduces some large discontinuities, especially in the unstructured grids, when the airfoil closure cannot be smoothly gridded in detail. In the geometry modeling the cylindrical hub has been extended to connect the two blades.

The upwind configuration S has been used in the current analyses. Wind speed is varied from 7 to 25 m/s (0.021 to 0.074 Mach). The rotor RPM is 72, resulting in a hover tip Mach number, $R\omega/c$, of 0.112. The tip pitch is 3 deg., and there is no coning. The rotor radius is 5.029 m. Sequence S allowed for free transition on the blade, with no fixed tripping. The Reynolds number magnitude and variation over the blade generally portend the existence of some laminar flow. Recent advances in transition methodologies [18] have shown some improved capability for prediction of the effects of transition on rotor blades. In this work the flow is assumed fully turbulent. Sequence M had leading edge transition fixed at 2% upper surface and 5% lower surface, but this dataset has yet to be evaluated to help determine the transition effects on the Phase VI rotor.

The Phase VI rotor is a stall-regulated turbine with the power generated being limited due to rotor stall. As the wind speed and, therefore, the section angles of attack, increase the stall on the rotor increases, further limiting the torque. This is opposed to a pitch-regulated wind turbine where the power generated is limited by changing the pitch of the blades. The flow regime generally remains attached, although active stall can also be employed [38]. From a CFD analysis standpoint, the stall regulated regime is particularly challenging. It requires accurate turbulence and transition models to correctly predict the stall initiation and development. As the Results section will show CFD does a poor job of predicting this behavior given the massive separated regions. Even in 2D, CFD and modern turbulence models have not shown to be completely reliable for prediction of stall angle of attack.

## IV. Results

CFD calculations have been performed for the NREL Phase VI rotor tested in the NASA Ames National Full-Scale Aerodynamics Facility (NFAC) Unsteady Aerodynamics Experiment. Results are compared for the range of NSU3D unstructured grids described as well as both OVERFLOW 2.1 and OVERFLOW-D. Integrated and detailed aerodynamic results are compared: aerodynamic torque and thrust, span loading, surface pressures, and surface and volume streamlines.

### A. Flow Solver Convergence and Scalability

Sample steady-state convergence characteristics are shown in Figure 6 and Figure 7 for NSU3D and OVERFLOW, respectively, for 7 and 25 m/s wind speed. For NSU3D, reasonable thrust and torque convergence is achieved after 10,000 to 15,000 iterations, depending on the wind speed on the fine mixed element mesh. For OVERFLOW torque convergence is obtained after 5,000 iterations for the low wind speed. The solution is unsteady at the high wind speed and does not converge. For the higher wind speeds with more stall, torque convergence is usually seen to be oscillatory. Some of these cases may in fact not be steady and should be run time-accurately. The coarse NSU3D grids showed better convergence for the attached flow cases, typically 6,000 iterations. On most of the NSU3D grids it was not possible to use more than two levels of multigrid, which would have significantly improved the convergence rates independent of grid size. In general, the Roe scheme was more stable, showed better convergence, and sometimes allowed the use of more multigrid levels.

Both NSU3D and OVERFLOW have shown good parallel processing scalability on problems of varying size. However, whereas OVERFLOW scalability tends to degrade when there are less than approximately 200,000 points per processor, NSU3D scalability is still good with as few as several thousand points per processor. NSU3D scalability on the finest grid (15.7M nodes) is shown in Figure 8 on up to 1024 processors, using a baseline time on 32 processors. Note that on 1024 processors there are only 15,000 points per processor. These results were obtained on an IBM Power 5+ with distributed memory and 16-processor nodes using MPI. NSU3D has shown super-linear scalability if a mix of OpenMP and MPI are employed on a shared memory machine [40].

### B. Aerodynamic Torque and Thrust

Rotor performance predictions are shown in Figure 9 for the Phase VI rotor for a range of wind speeds. Results are dimensional. Elsewhere in the paper non-dimensional thrust and torque coefficients may be used, with non-dimensionalization by the rotor hover tip speed, $R\omega$. All the meshes accurately predict the attached flow 7 m/s case for torque, although the thrust is somewhat overpredicted. Note that while the torque measurements are made from strain gauges, the thrust measurements are estimated from the integrated airloads at the 5 instrumented pressure stations. Beyond ~9 m/s wind speed the rotor enters the stall-regulated portion of the performance curve. However, most of the unstructured grids with the Spalart-Allmaras turbulence model predict the stall too late (> 10-13 m/s). The coarser grids do predict the stall at 10 m/s and are, therefore, in better agreement with the data, however, this is fortuitous as they clearly do not show grid convergence compared with the finer grids. The finer unstructured grids all overpredict the torque at 10 and 13 m/s. The unstructured mesh with refined normal spacing showed no differences. The OVERFLOW-D results are consistent with the fine unstructured results although the OVERFLOW 2.1 results predict stall sooner and deeper. The OVERFLOW-D results here with the Baldwin-Barth turbulence model do not show the excellent agreement seen in Ref. 3. At wind speeds higher than 15 m/s, all the fine grid results are in overall good agreement with the data. The Roe scheme is somewhat more accurate than the matrix dissipation scheme on the same mesh, but this may be due to a higher level of dissipation rather than a more accurate discretization [10]. The exception to these remarks is the unstructured grid generated from the structured surface mesh. This grid drastically overpredicts the torque. This is most likely due to the excessive surface cell aspect ratio which the unstructured flow solver does not handle well. Also, neither of the fully triangular surface grid meshes perform very well compared with OVERFLOW or the mixed element surface fine grids. This may be due to the difficulty of accurately resolving the geometry using unstretched, uniform triangular cells without excessive node count. Differences have also been seen in Ref. 10 between grids with and without spanwise stretching.

Overall, all the grids predicted the attached flow; none correctly identified the correct location of stall; and most handled the post-stall region reasonably well. Except at 10 m/s, the OVERFLOW 2.1 results appears to be in best agreement with the data. The Roe scheme on the fine mixed element surface mesh performed moderately better than the other unstructured fine grids and algorithms. The unstructured meshes can seemingly match the accuracy of the structured mesh given the same resolution, but without the ability to handle large cell aspect ratios the surface cell count increases dramatically in order to maintain reasonable streamwise spacing (leading and trailing edges). The poor prediction of stall onset is most likely attributable to the Spalart-Allmaras turbulence model and lack of transition modeling. Researchers using the Menter k-ω SST model have shown reasonable prediction of the stall initiation at 10 m/s wind speed but tend to underpredict the torque at higher wind speeds [5,28].

### C. Spanload Distributions

The spanload distributions of the sectional forces contributing to thrust, $c_{th}$, and torque (driving force), $c_{tq}$, are shown in Figure 10 for a range of wind speeds. At 7 m/s the torque force distribution is well predicted, although the

thrust is generally overpredicted, as noted in the inset in Figure 9. OVERFLOW and the NSU3D Roe scheme do the best job of thrust prediction. At 10 m/s none of the results capture the large torque loss in the mid-span region, due to incorrect stall prediction. This is the major cause of the inability of CFD and the turbulence model to correctly predict initiation of the stall-regulated regime. The thrust distribution is also overpredicted. At the fully stalled 25 m/s condition, the torque force distributions are in good agreement with the data. The shape of the thrust distributions indicate higher loading outboard and reduced loading inboard compared with the data. While the mean thrust may average out, errors in the distribution of this manner would adversely affect prediction of root bending moment.

### D. Surface Pressure Distributions

Surface pressure distributions are shown in Figure 11 for 7, 10, and 25 m/s wind speeds. In the experimental data, the stagnation point dynamic pressure is used for non-dimensionalization. The calculations use a dynamic pressure based on a combination of the wind speed and local rotor section speed, $1/2\,\rho[v_\infty^2 + (r\omega)^2]$. As indicated by the integrated thrust and torque results, the meshes with unstretched triangular surface grids do not perform particularly well and will no longer be discussed. At 7 m/s the calculated pressure distributions are in good agreement with the test data. At 10 m/s the overprediction of the stall angle is evident in the 47% span station where the test data indicates significant separation. At the inboard 30% station the different grids and results show varying degrees of separation. The flow is mostly attached at the outboard station and is in good agreement with the data. Near the trailing edge the different grids indicate small and varying amounts of separation. At 25 m/s the entire blade is separated. Pressure predictions are generally good in the separated regions, with some discrepancy in the pressure level and the upper surface aft region inboard. Details of the separation patterns seen in the pressure distributions will be explored in the next section.

Of note in the pressure distributions are the significant oscillations along the chord, especially at the inboard sections. This is most likely a numerical low Mach number effect. Without any preconditioning, the pressure will be under-dissipated, while the velocity will be over-dissipated. OVERFLOW does not seem as susceptible to these pressure oscillations, and the NSU3D Roe scheme is similarly less affected compared with the matrix dissipation scheme. The other notable effect is the very large trailing edge spikes. This is due to the original geometry definition and the attempt to close off the open/blunt trailing edge too quickly. The unstructured grids exacerbate the problem because compared with the structured grid they have much coarser trailing edge spacing and the closure is more drastic.

### E. Surface and Flow Field Streamlines

Surface streamlines (oil flow) with surface pressure distributions are shown in Figure 12 for the OVERFLOW and the NSU3D central difference fine grid results at 7, 10, 15, and 25 m/s wind speed. As indicated in the integrated forces and pressure distributions, the flow is generally attached at 7 m/s, moderately separated at 10 m/s, almost fully separated except for the tip at 15 m/s, and completely separated at 25 m/s. Quantitative agreement between the two codes is quite good. OVERFLOW shows a small amount of trailing edge separation at 7 m/s which is not present in the NSU3D results. This reversed flow region is confined very close to the surface ($1.0\text{x}10^{-4}$ m) and in the region where the trailing edge abruptly closes. It is probably not present in the NSU3D result due to reduced trailing edge chordwise grid spacing. At 15 m/s where the OVERFLOW integrated performance results indicate lower torque and thrust due to increase stall, there are comparable differences in the surface streamlines and pressures. In general, in regions of incipient separation near the trailing edge (7 m/s inboard) the radial component of the flow increases, and in areas of fully separated flow the radial flow is completely dominant. Figure 13 shows the significant off-surface extent of the separated flow region at 47% span for the 13 m/s wind speed. The OVERFLOW results separated earlier, so there is a larger separated region and reduced torque.

### F. Time-Accurate Calculations

For comparison with the non-inertial, fixed mesh, steady-state formulation, a sample calculation has been performed in a time accurate manner. This is necessary for future work involving bodies in relative motion, such as rotor-ground-tower calculations. The coarse mixed element surface mesh has been used. In the moving mesh formulation, the complete mesh rotates at the specified speed, as opposed to an overset formulation where the blade meshes might move through a stationary background mesh. A time step study determined that a time step equivalent

to 0.32 deg (1125 time steps per rotor revolution) using 20-40 subiteration offers a good compromise between solution accuracy and efficiency. Larger time steps require significantly more subiterations at each time step, while smaller time steps do not noticeably improve the accuracy and offer only minor reduction in the number of subiterations required to reach force and moment convergence at each step. Three levels of multigrid are used at each time step for inner convergence and showed significant improvement over less or no multigrid. Larger numbers of multigrid levels were not stable. The time-accurate calculation was initiated using a reduced number of subiterations (10) to speed convergence over the initial transients. Figure 14a shows the thrust and torque convergence histories and verification of time step and subiteration convergence. Figure 14b shows that at each time step 1.5-2.0$^{+}$ orders of magnitude reduction in the residual is obtained with 20-40 subiterations. Compared with the steady-state formulation on the same mesh at the same conditions (10 m/s), the thrust and torque are within less than 0.2%. The time-accurate solution requires approximate 2 rotor revolutions to reach convergence. At 1125 steps per revolution and an average of 20 subiterations each, this is almost three times as expensive as the steady-state formulation on this grid, which required 8000 iterations.

### G. Unstructured Mesh Adaption and Wake Resolution

For accurate and efficient CFD calculations it is useful to know the distance downstream that the wake must be resolved. Manual and automatic adaptive refinement have been used to better capture the wind turbine wake in order to determine the sensitivity of the turbine performance to wake resolution. The adaption strategy described in the Methodology section is applied to the coarse grid with unstructured mixed element surface mesh at 10 m/s wind speed. Three adaption levels are employed. All levels adapt to a Q criteria value of $4x10^{-6}$ $s^{-2}$, based on the units of the flow solver (grid in meters, velocity non-dimensionalized by $v_{\infty}$). The value was determined visually, and further research is required to fully automate the feature detection process. The first adaption also adapted to velocity gradient across edges. The initial grid was manually adapted in the wake using the wake source sheet in AFLR, as shown in Figure 3. Successive adaptions continually resolve the hub and tip vortices, as shown in Figure 15 and Figure 16. No adaption was performed in the prism layers of the grid, only in the tetrahedral cells, so that no surface adaption was performed. Each new adapted grid was run in the flow solver from freestream initial conditions. Based on the difficulties explained in the Methodology section, the AMR technology requires further development and validation for robustness.

Mesh details and performance prediction from the 4 grids are shown in Table 2. By the second and third adaption levels the performance predictions have leveled off. In this case the final mesh adaption has resolved ¾ of a revolution of the tip vortex. For a 10 m/s wind speed, this is a distance of 1.25R downstream. Considerably more of the hub vortices are captured. Note that the unadapted coarse mesh can barely resolve ¼ of a revolution with an extremely diffused tip vortex. Even with the edge count modification to the flow solver, the central difference scheme did not obtain a converged solution on the final adapted mesh. The Roe scheme, however, did converge on all meshes. The downstream resolution conclusions where the same with both schemes.

The wake resolving ability of the second-order unstructured solver is considerably worse than solvers using Cartesian meshes in the wake, sometimes in conjunction with higher-order spatial algorithms [3,4,35]. The OVERFLOW result was also able to capture up to 1.25R of the tip vortices downstream, but without any downstream grid resolution or wake adaption. In the CFD calculations, the resolved distance downstream is a somewhat subjective measure based on the vorticity contours chosen. Results by Zahle [35] are particularly impressive in their ability to resolve more than 12R downstream with minimal dissipation and a second-order scheme. In that work it was determined that it was only necessary to resolve the detailed wake vortex structure one rotor radius downstream of the rotor in order to predict the induction and rotor performance, a conclusion in agreement with the current work.

## V. Conclusions

Computational fluid dynamics calculations have been performed on the NREL Phase VI Unsteady Aerodynamics Experiment. An isolated rotor configuration has been analyzed with an unstructured mesh solver NSU3D and compared with a well-validated overset, structured mesh solver OVERFLOW and wind tunnel test data. The following conclusions are made:

1. Using the Spalart-Allmaras turbulence model the initiation of the stall-regulated portion of the torque curve is overpredicted and delayed. Thrust is reasonably well predicted. Further work with other turbulence models is required.

2. Convergence of the unstructured flow solver requires 8000-15000 iterations for the steady-state formulation on fine meshes. Increased multigrid levels can, when stable, improve the convergence rate. The steady-state formulation is significantly more efficient than an unsteady calculation, while resulting in essentially the same performance predictions. The unsteady formulation is required for modeling ground planes, non-uniform inflow, nacelles, and towers.
3. The unstructured solver can generate results that compare well to a structured grid solver. However, without the ability to handle large aspect ratio cells on the blade surface, the node count may not be comparable.
4. Low Mach number aspects of the flow resulted in oscillatory surface pressures in the unstructured solver. A correct low Mach number preconditioning formulation for moving meshes is required, and should result in more accurate and efficient solutions.
5. The Roe scheme with least squares gradient reconstruction shows more favorable convergence, robustness, smoothness, and low Mach number properties than the central difference scheme with artificial dissipation.
6. Resolving the wake 1.25 rotor radii downstream results in convergence of the rotor performance. Grid adaption can successfully be used as an efficient means of resolving the wake and resulting in reduced node count. Issues regarding appropriate adaption parameters and adapted grid quality require further research.

## VI. Acknowledgements

The authors thank Dr. Earl Duque for the Phase VI overset mesh. Dr. Scott Schreck at NREL kindly provided the UAE data. The first author is especially grateful for support under the AMRDEC Expanded Development Opportunity (Sabbatical) Program and the University of Wyoming Wind Energy Research Center.

## References

[1] Hand, M. M., Simms, D. A., Fingersh, L. J., Jager, D. W., Cotrell, J. R., Schreck, S. J., and Larwood, S. M., "Unsteady aerodynamics experiment phase VI: wind tunnel test configurations and available data campaigns," NREL/TP-500-29955, December 2001.

[2] Schreck S., "Unsteady aerodynamics experiment wind tunnel database," www.nrel.gov/uaewtdata, 2004.

[3] Duque, E. P. N., Burklund, M. D., and Johnson, W., "Navier–Stokes and comprehensive analysis performance predictions of the NREL phase VI experiment," *Journal of Solar Energy Engineering* 2003; 125: 457–467.

[4] Chao, D. D., and van Dam, C. P., "Computational Aerodynamic Analysis of a Blunt Trailing-edge Airfoil Modification to the NREL Phase VI Rotor," *Wind Energy*, July 2007, 10:529-550.

[5] Le Pape, A., and Gleize, V., "Improved Navier-Stokes Computations of a Stall-Regulated Wind Turbine Using Low Mach Number Preconditioning," 44th AIAA Aerospace Sciences Meeting and Exhibit, Reno, NV, January 2006, AIAA 2006-1502.

[6] Gonzalez A., and Munduate, X., "Three-dimensional and Rotational Aerodynamics on the NREL Phase VI Wind Turbine Blade," 45th AIAA Aerospace Sciences Meeting and Exhibit, Reno, NV, January 2007, AIAA 2007-0628.

[7] Schmitz, S., and Chattot, J-J., "Application of a 'Parallelized Coupled Navier-Stokes/Vortex Panel Solver' to the NREL Phase VI Rotor," 43rd AIAA Aerospace Sciences Meeting and Exhibit, Reno, NV, January 2003, AIAA 2003-0593.

[8] Zahle, F., Johansen, J., Sorenson, N., and Graham, J., "Wind Turbine Rotor-Tower Interaction Using an Incompressible Overset Grid Method," AIAA 45th Aerospace Sciences Meeting and Exhibit, Reno, NV, January 2007, AIAA 2007-0425.

[9] Mavriplis, D. J., "Multigrid Strategies for Viscous Flow Solvers on Anisotropic Unstructured Meshes," *Journal of Computational Physics*, Vol. 145, No. 1, Sept. 1998, pp. 141–165.

[10] Mavriplis, D., "Unstructured Mesh Discretizations and Solvers for Computational Aerodynamics," *AIAA Journal*, Vol. 46, No. 6, June 2008, pp. 1281-1298.

[11] Mavriplis, D., "Third Drag Prediction Workshop Using the NSU3D Unstructured Mesh Solver," *AIAA Journal of Aircraft*, Vol. 45, No. 3, March 2008, pp. 750-761.

[12] Mavriplis, D., "Adaptive Meshing Techniques for Viscous Flow Calculations on Mixed Element Unstructured Meshes," *International Journal for Numerical Methods in Fluids*, Vol. 34, No.2, September 2000, pp. 93-111.

[13] http://www.pointwise.com/pw.

[14] Marcum, D. L., and Gaither, J. A., "Mixed Element Type Unstructured Grid Generation for Viscous Flow Application," 14th AIAA Computational Fluid Dynamic Conference, Norfolk, VA, June 1999, AIAA 1999-3252.

[15] Jeong, J., and Hussain, F., "On the Identification of a Vortex," *Journal of Fluid Mechanics*, Vol. 285, 1985, pp. 69-94.

[16] Larsen, J., "ANSYS CFD Applied to Wind Turbines at Siemens Wind Power," ANSYS Conference & 26th CADFEM Users' Meeting, Darmstadt, Germany, October 2008.

[17] Standish, K., "CFD at GE", WindPower 2007, Los Angeles, CA, June 2007.

[18] Langtry, R. B., Gola, J., and Menter, F. R., "Predicting 2D Airfoil and 3D Wind Turbine Rotor Performance using a Transition Model for General CFD Codes," 44th AIAA Aerospace Sciences Meeting and Exhibit, Reno, NV, January 2006, AIAA-2006-395.

[19] Johansen J., Madsen, H. A., Sørensen, N. N., and Bak C., "Numerical Investigation of a Wind Turbine Rotor with an Aerodynamically Redesigned Hub-Region," 2006 European Wind Energy Conference and Exhibition, Athens, Greece, 2006.

[20] Johansen J., and Sørensen N. N.: "Aerodynamic investigation of winglets on wind turbine blades using CFD", Risø-R-1543(EN) report 2006.

[21] Hansen, M. O. L., and Johansen, J., "Tip Studies Using CFD and Comparison with Tip Loss Models," *Wind Energy*, 2004, p. 343 -356.

[22] Park, Y. M., Chang, B-H., and Cho, W-H., "Numerical Simulations of Wind Turbine Scale Effects Using CFD," 45th AIAA Aerospace Sciences Meeting and Exhibit, Reno, NV, January 2007, AIAA-2007-216.

[23] Simms, D. A., Schreck, S., Hand, M., and Fingersh, L., J., "NREL Unsteady Aerodynamics Experiment in the NASA-Ames Wind Tunnel: A Comparison of Predictions to Measurements" NREL/TP-500-29494, June 2001.

[24] Standish, K. J., and van Dam, C. P., "Aerodynamic Analysis of Blunt Trailing Edge Airfoils," *Journal of Solar Energy Engineering* ,Vol. 125, No. 4, Nov. 2003, pp. 479–487.

[25] Fuglsang, P., and Bak, C., "Development of the Risø Wind Turbine Airfoils," *Wind Energy*, Vol. 7. No. 2, May 2004, p. 145-162.

[26] Hjort, S., Laursen, J., and Enevoldsen, P., "Aerodynamic Winglet Optimization," Sandia National Lab Blade Workshop, May 2008.

[27] U. S. Dept. of Energy, "20% Wind Energy by 2030: Increasing Wind Energy's Contribution to U.S. Electricity Supply," July 2008, http://www.nrel.gov/docs/fy08osti/41869/pdf.

[28] Sørensen, N. N., Michelsen, J. A., and Schreck, S., "Navier-Stokes Predictions of the NREL Phase VI rotor in the NASA Ames 80ft x120 ft wind tunnel," *Wind Energy*, Vol. 5, No. 2-3, 2002, pp. 151-169.

[29] Johansen, J., Sørensen, N. N., Michelsen, J. A., and Schreck, S., "Detached-Eddy Simulation of Flow around the NREL Phase-VI Rotor," *Wind Energy*, Vol. 5, No. 2-3, 2002, pp. 185-197.

[30] Wang, X., Sheng, C., and Chen, J. P., "Numerical Study of Preconditioned Algorithm for Rotational Flows," 17th AIAA Computational Fluid Dynamics Conference, Toronto, Canada, June 2005, AIAA 2005-5126.

[31] Nichols, R. H., "Algorithm and Turbulence Model Requirements for Simulating Vortical Flows," AIAA 46th Aerospace Sciences Meeting and Exhibit, Reno, NV, January 2008, AIAA 2008-0337.

[32] Nichols, R., Tramel, R., and Buning, P., "Solver and Turbulence Model Upgrades to OVERFLOW 2 for Unsteady and High-Speed Applications," AIAA 24th Applied Aerodynamics Conference, San Francisco, CA, June 2006, AIAA 2006-2824.

[33] Buning, P., " Consolidation of Time-Accurate, Moving Body Capabilities in OVERFLOW", 6th Overset Composite Grid and Solution Technology Symposium, Ft. Walton Beach, FL, October 2002.

[34] Chan, W. M., Meakin, R. L., and Potsdam, M. A., "CHSSI Software for Geometrically Complex Unsteady Aerodynamic Applications," AIAA 39th Aerospace Sciences Meeting and Exhibit, Reno, NV, January 2001, AIAA 2001-0593.

[35] Zahle, F., and Sørensen, N. N., "On the Influence of Far-Wake Resolution on Wind Turbine Flow Simulations," *Journal of Physics: Conference Series*, The Science of Making Torque from Wind, Lyngby, Denmark, August 2007.

[36] Mavriplis, D., and Yang, Z., "Construction of the Discrete Geometric Conservation Law for High-Order Time-Accurate Simulations on Dynamic Meshes," *Journal of Computational Physics*, Vol. 213, No. 2, April 2006, pp. 557-573.

[37] Kang, H. J., and Kwon, O. J., "Effect of Wake Adaptation on Rotor Hover Simulations Using Unstructured Meshes," Journal of Aircraft, Vol. 38, No. 5, Sept.-Oct. 2001, pp. 868-877.

[38] Hansen, M. O., Aerodynamics of Wind Turbines, London: Earthscan, 2008.

[39] Chen, J. P., Gosh, A. R., Sreenivas, K., and Whitfield, D. L., "Comparison of Computations using Navier-Stokes Equations in Rotating and Fixed Coordinates for Flow through Turbomachinery," AIAA 35th Aerospace Sciences Meeting and Exhibit, Reno, NV, January 1997, AIAA 98-0878.

[40] Mavriplis, D., Aftosmis, M., and Berger, M., "High-Resolution Aerospace Applications using the NASA Columbia Supercomputer," *International Journal of High Performance Computing Applications*, Vol. 21, No. 1, pp. 106-126, 2007.

[41] Karypis, G., and Kumar, V., "A Fast and High Quality Multilevel Scheme for Partitioning Irregular Graphs," *SIAM Journal on Scientific Computing*, Vol. 20, No. 1, pp. 359-392, 1999.

| surface mesh topology | surface points | nodes | cells |
|---|---|---|---|
| triangulated multiblock | 21,916 | 1.2 M | 3.2 M |
| triangular unstructured | 60,415 | 2.8 M | 6.7 M |
| fine triangular unstructured | 364,440 | 8.3 M | 21.8 M |
| mixed element unstructured | 67,017 | 3.2 M | 7.9 M |
| fine mixed element unstructured | 496,548 | 12.5 M | 32.5 M |
| fine mixed element unstructured with reduced normal spacing | 496,548 | 15.7 M | 38.3 M |
| overset structured | 51,034 | 6.0 M | |

**Table 1. Mesh sizes**

| | Thrust | Torque | Nodes | Cells |
|---|---|---|---|---|
| unadapted | 1970 | 1521 | 3.2 M | 7.9 M |
| adapt 1 | 1893 | 1460 | 3.8 M | 11.0 M |
| adapt 2 | 1878 | 1446 | 4.7 M | 16.3 M |
| adapt 3 | 1854 | 1426 | 8.6 M | 39.7 M |

**Table 2. Grid adaption, coarse grid – mixed element surface, v = 10 m/s**

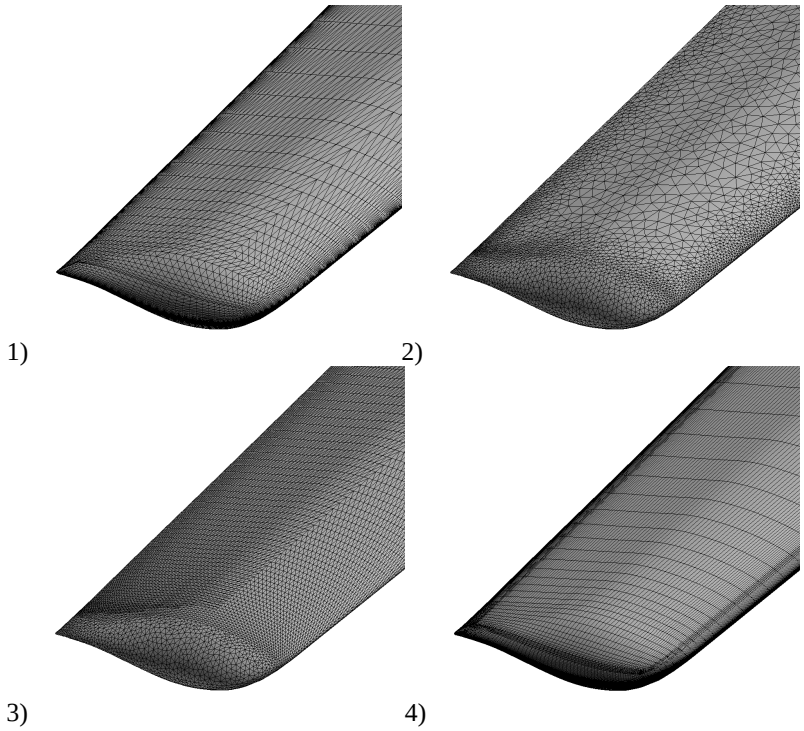

1) 2)

3) 4)

**Figure 1. Unstructured surface mesh topologies: 1) triangulated structured multiblock, 2) fully unstructured triangular, 3) mixed element, 4) overset, structured**

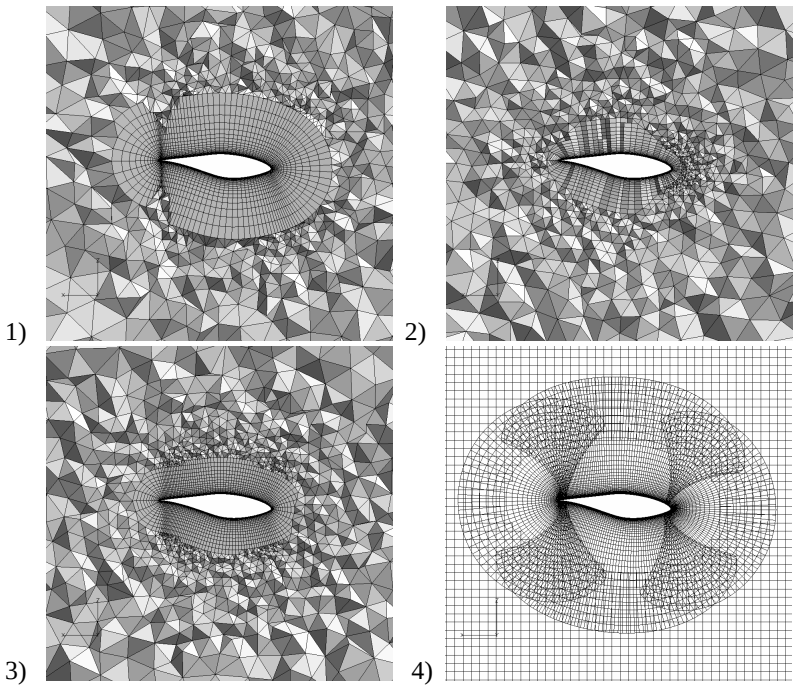


**Figure 2. Volume meshes for surface topologies: 1) triangulated structured multiblock, 2) fully unstructured triangular, 3) mixed element, 4) overset, structured**

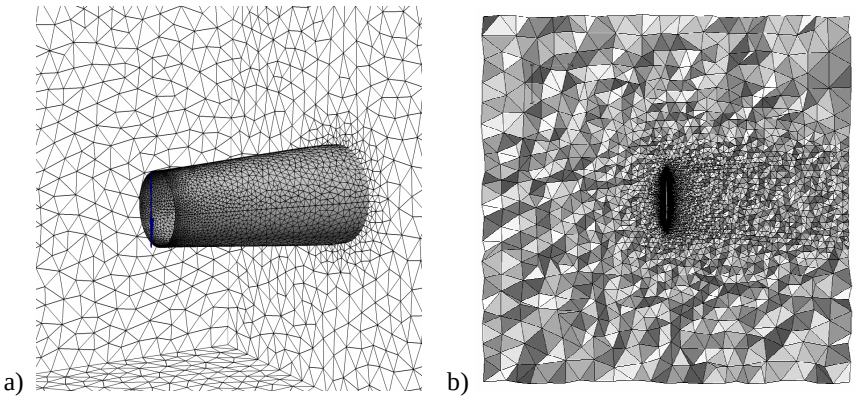


**Figure 3. Surface (a) and volume (b) unstructured meshes with manual wake clustering**

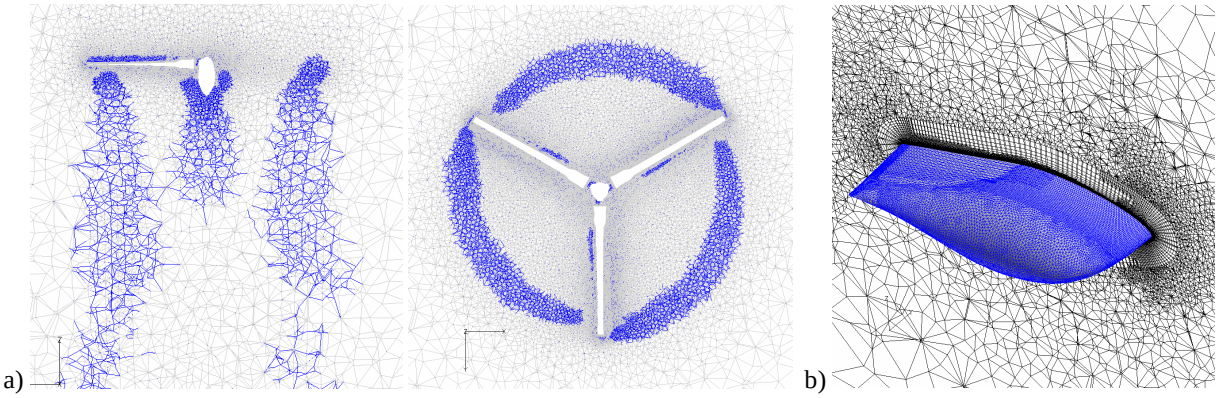


**Figure 4. Adaptive mesh refinement: a) isolated rotor in hover (side, top view), and b) wind turbine blade tip**

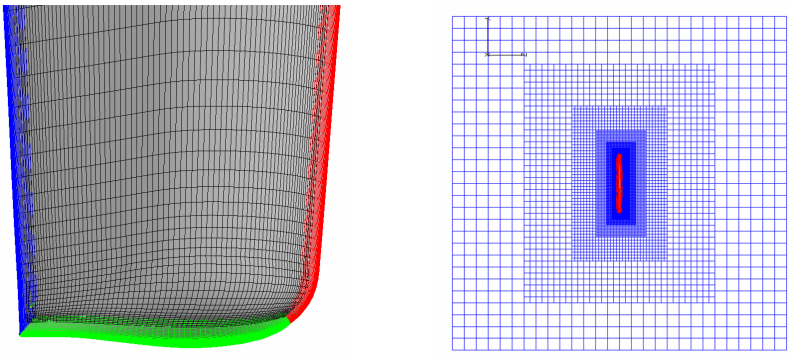

**Figure 5. Structured overset mesh surface (blade tip) and volume grid**

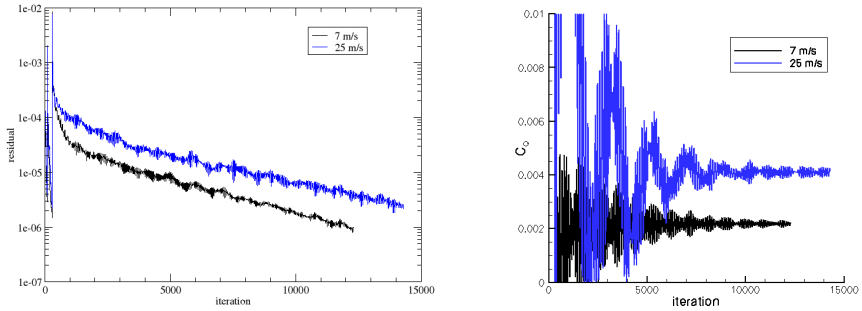


**Figure 6. NSU3D residual and torque convergence, fine 12.5 M node grid, v = 7 and 25 m/s**

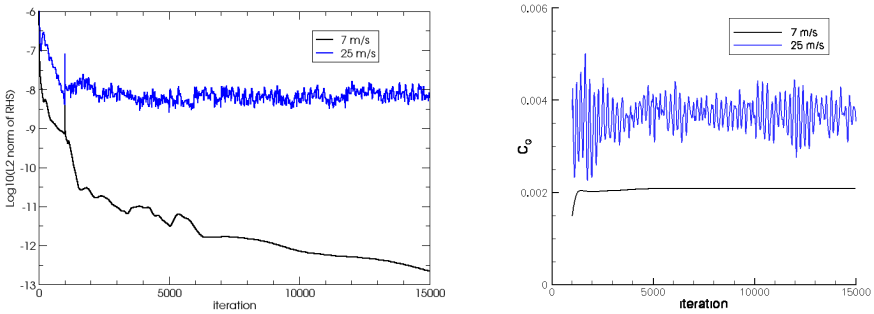


**Figure 7. OVERFLOW 2.1 residual and torque convergence, v = 7 and 25 m/s**

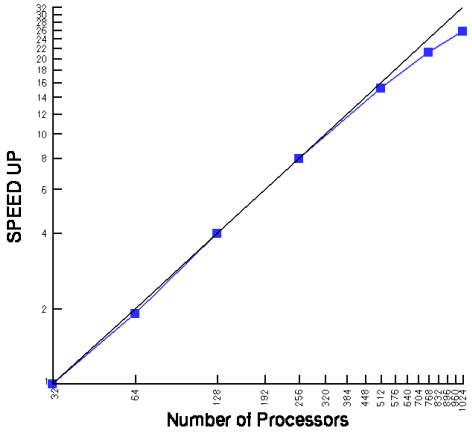


**Figure 8. NSU3D MPI scalability, 15.7 M node mesh, up to 1024 processors, compared with linear**

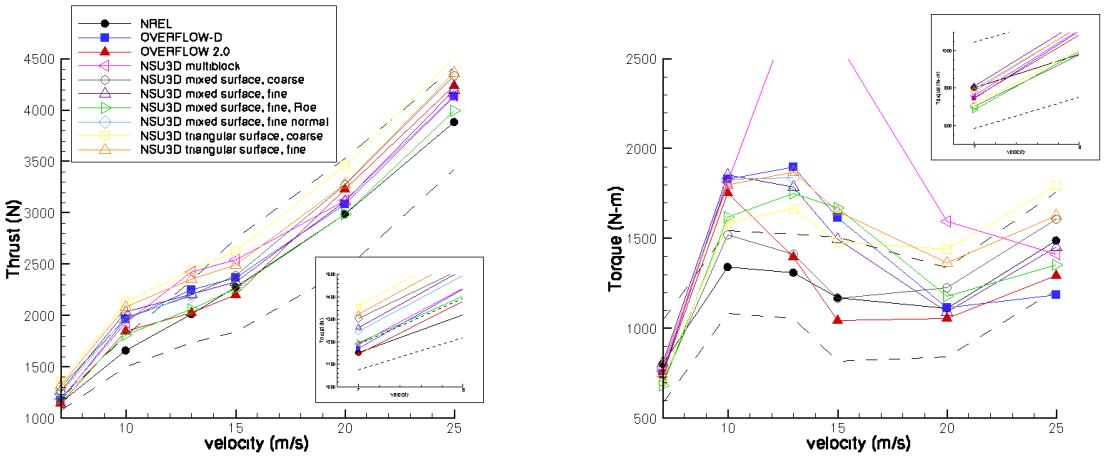


**Figure 9. NREL Phase VI rotor performance predictions, thrust and torque**

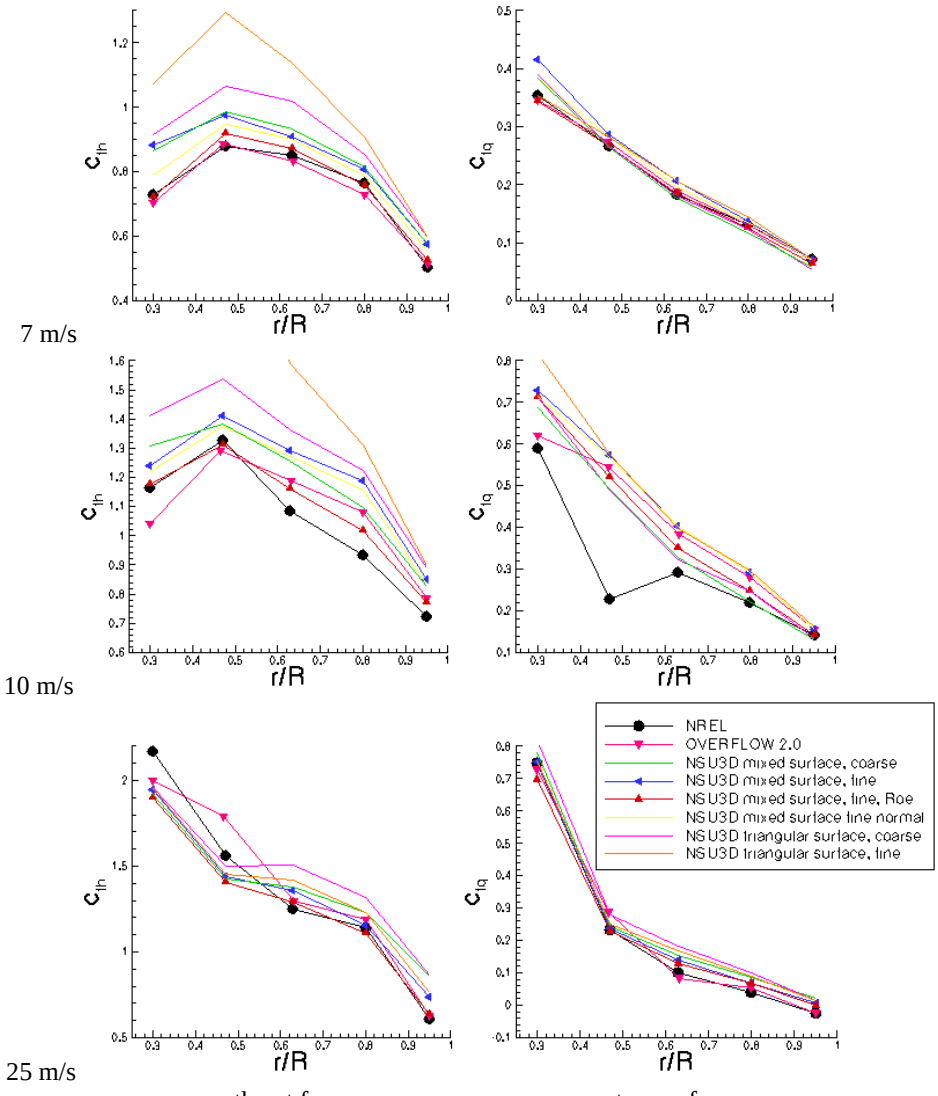


**Figure 10. Thrust and torque force distributions along the span, v = 7, 10, 25 m/s**

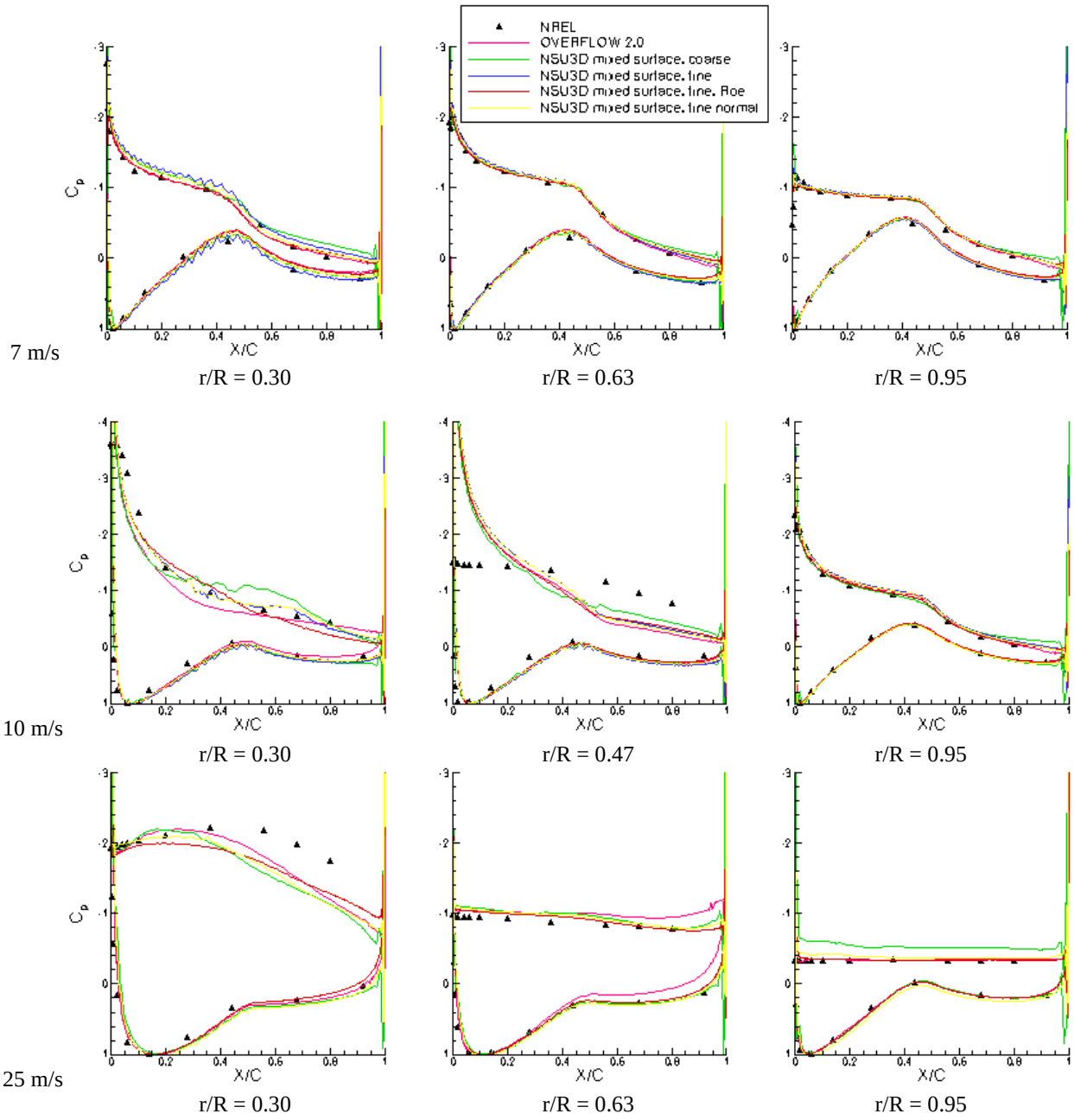


**Figure 11. Section pressure distributions, v = 7, 10, 25 m/s, r/R = 0.30, 0.47/0.63, 0.95**

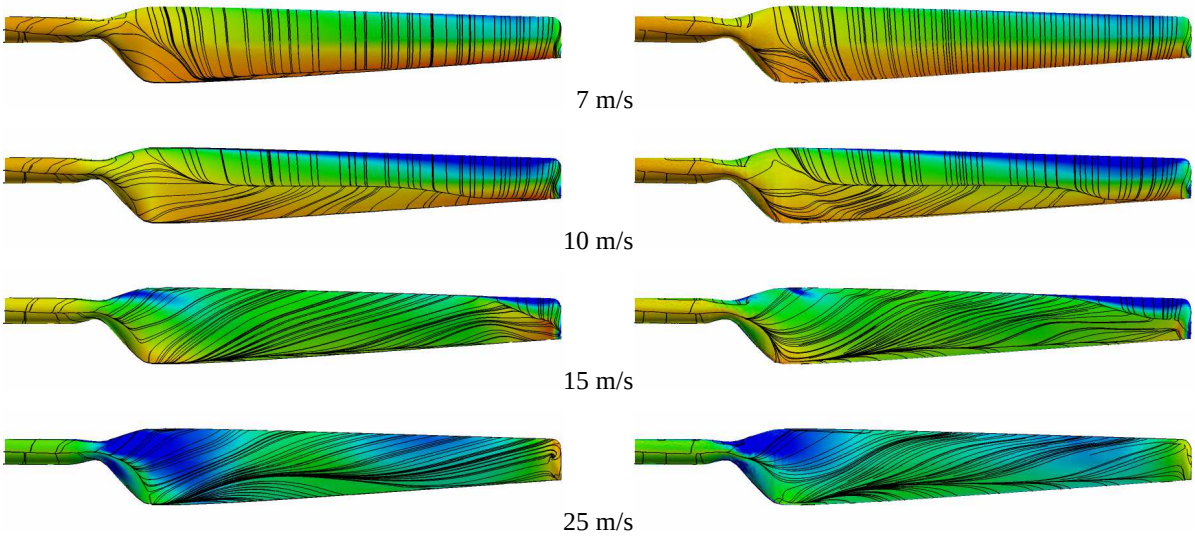


**Figure 12. Surface streamlines, v = 7, 10, 15, 25 m/s**

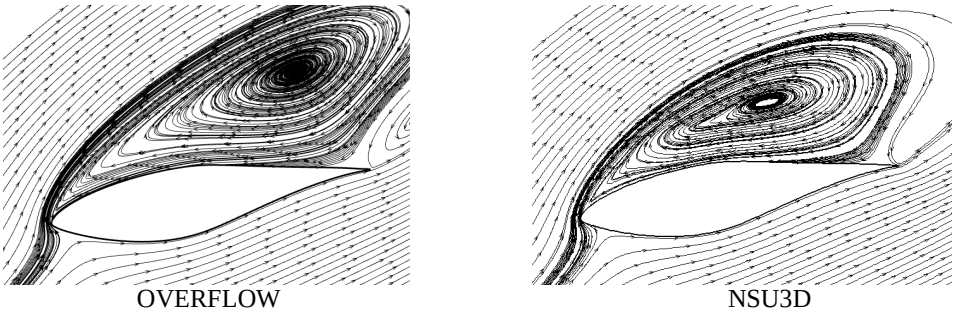


**Figure 13. Flow field separation, v = 13 m/s, r/R = 0.47**

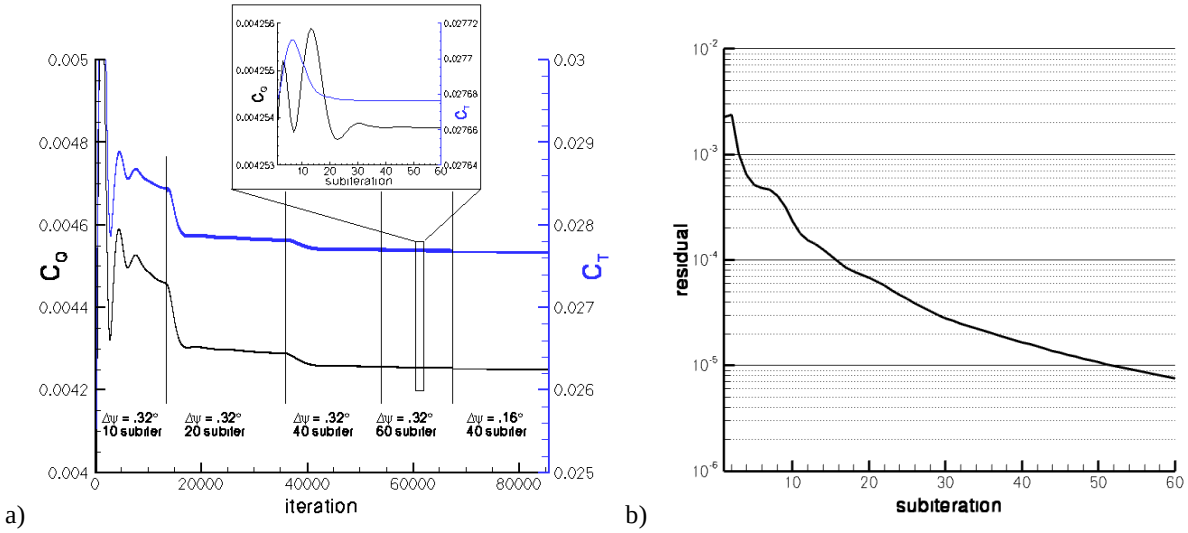


**Figure 14. Time accurate convergence of a) solution and subiteration thrust and torque, and b) subiteration residual (Δψ = 0.32°), coarse grid, v = 10 m/s**

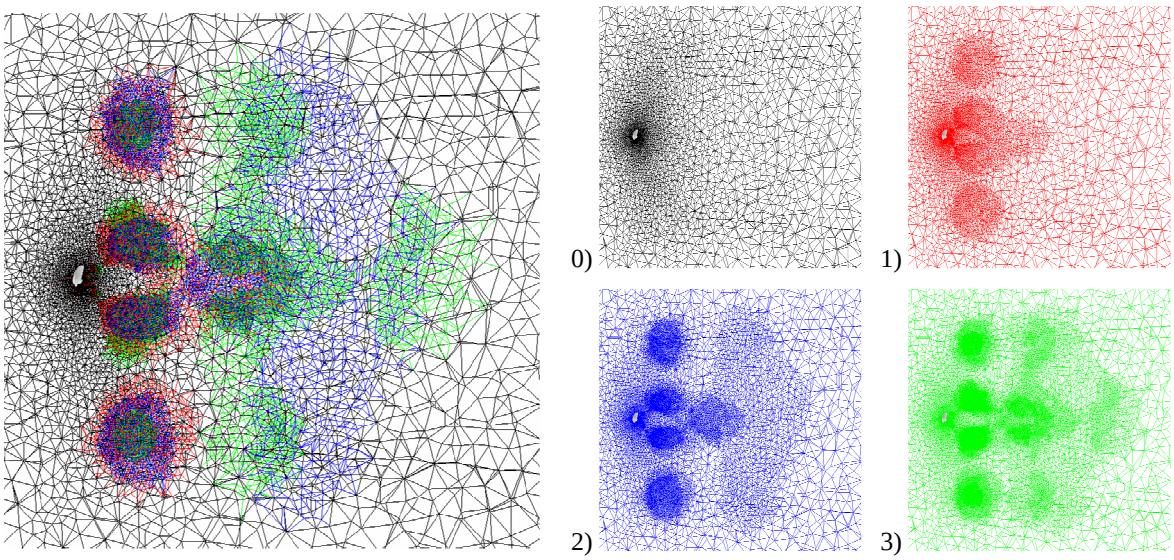


**Figure 15. Unstructured adaptive mesh refinement in the wake on plane perpendicular to the rotor, coarse grid, adaption levels 0 (initial), 1 (red), 2 (blue) , 2 (green), v = 10 m/s**

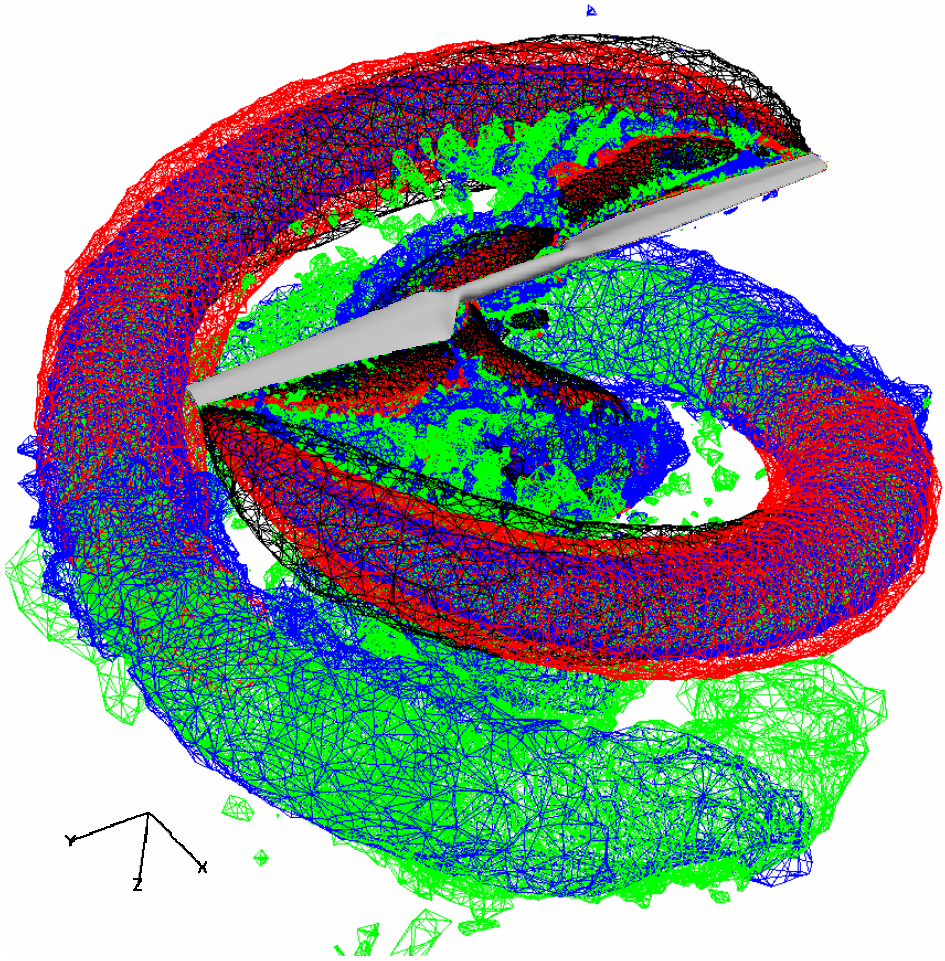


**Figure 16. Unstructured adaptive mesh refinement, iso-surface of Q-criteria depicting hub and tip vortices, adaption levels 0 (initial), 1 (red), 2 (blue), 2 (green), v = 10 m/s**